Letter

# Self-Assembled Au Nanoelectrodes: Enabling Low-Threshold-Voltage HfO$_2$-Based Artificial Neurons

Hongyi Dou,* Zehao Lin, Zedong Hu, Benson Kunhung Tsai, Dongqi Zheng, Jiawei Song, Juanjuan Lu, Xinghang Zhang, Quanxi Jia, Judith L. MacManus-Driscoll, Peide D. Ye, and Haiyan Wang*

Cite This: https://doi.org/10.1021/acs.nanolett.3c02217

Read Online

ACCESS | Metrics & More | Article Recommendations | SI Supporting Information

**ABSTRACT:** Filamentary-type resistive switching devices, such as conductive bridge random-access memory and valence change memory, have diverse applications in memory and neuromorphic computing. However, the randomness in filament formation poses challenges to device reliability and uniformity. To overcome this issue, various defect engineering methods have been explored, including doping, metal nanoparticle embedding, and extended defect utilization. In this study, we present a simple and effective approach using self-assembled uniform Au nanoelectrodes to controll filament formation in HfO$_2$ resistive switching devices. By concentrating the electric field near the Au nanoelectrodes within the BaTiO$_3$ matrix, we significantly enhanced the device stability and reduced the threshold voltage by up to 45% in HfO$_2$-based artificial neurons compared to the control devices. The threshold voltage reduction is attributed to the uniformly distributed Au nanoelectrodes in the insulating matrix, as confirmed by COMSOL simulation. Our findings highlight the potential of nanostructure design for precise control of filamentary-type resistive switching devices.

**KEYWORDS:** threshold switching, artificial neuron, defect engineering, vertically aligned nanocomposite, HfO$_2$
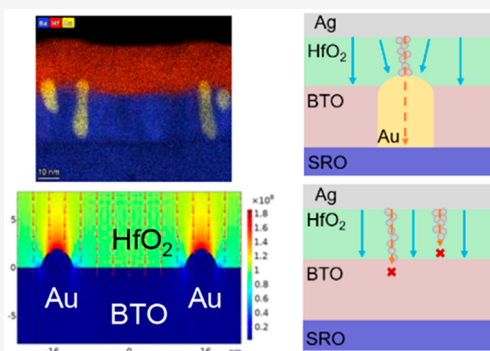
Neuromorphic computing is an innovative computing scheme that aims to emulate the biological processes of the human brain.[1] This type of computing offers several benefits over traditional computing methods, including low power consumption, real-time processing, scalability, and cognitive computing capabilities.[2−6] Resistive switching materials, mostly metal oxides including TiO$_2$,[7,8] TaO$_x$,[9] CeO$_2$,[10−12] HfO$_2$,[13] and SiO$_2$,[14−16] greatly advance the development and implementation of neuromorphic computing as they are capable of emulating either a neuron or a synapse with a single device.[5,17,18] In particular, filamentary-based devices such as conductive-bridge random-access memory (CBRAM) and resistive random-access memory (RRAM) have gained significant attention in recent years.[3,19−22] CBRAM uses active metal electrodes (Cu, Ag, etc.) to form metallic conducting filaments, while RRAM relies on the construction of conducting filaments using oxygen vacancies.[23−26] However, the stochastic nature of the filament formation process involving the hopping of active species can result in additional energy consumption and large variations in device performance, hindering the development of low-energy and highly reliable devices for artificial neurons and synapses.[27−30]

A range of defect engineering methods and structural designs have been employed to enhance the performance of resistive switching materials toward neuromorphic computing. These methods include utilizing dislocations and grain boundaries as transport channels,[31−35] doping,[36−42] embedding metal nanoparticles,[43−48] and special patterning of the top or bottom electrodes.[49,50] Among these methods, embedding metal nanoparticles and utilizing patterned electrodes have been recognized as highly effective approaches to enhance the control of filament formation and reduce the switching voltage by manipulating the electric field distribution in the oxide switching layer. However, the fabrication process associated with both methods tends to be complex and costly. They often require the use of additional templates, multiple rounds of e-beam or photolithography, and postdeposition treatment at high temperatures for extended durations.[51,52] Furthermore, patterned electrodes often have large dimensions, posing challenges for device scaling and integration with other on-chip components.[49,50] Therefore, a more efficient and effective method with a great scaling ability is needed to incorporate metal nanoparticles into the materials.

One promising approach for incorporating metal nanoparticles involves a self-assembling process during the growth
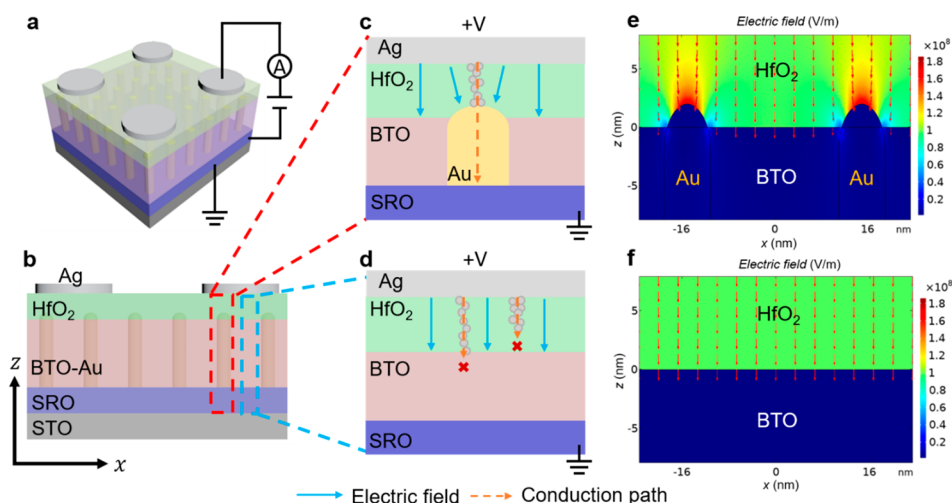
**Figure 1.** (a) Schematic illustration of the Ag/HfO$_2$/BTO−Au/SRO/STO device and measurement setup. (b) Schematic illustration of the cross-sectional view of the Ag/HfO$_2$/BTO−Au/SRO/STO device. z- and x-axes represent the out-of-plane and in-plane directions, respectively. (c, d) Schematic illustrations of the switching process in regions marked by the red and blue boxes in (b), respectively. (e, f) Corresponding COMSOL simulation of the electric field in (c) and (d).

of an insulating matrix. This can be achieved through the utilization of vertically aligned nanocomposites (VANs), which exhibit a vertical arrangement of two or more phases on a single substrate. A large range of oxide−oxide VANs have been investigated,[53−57] with recent advancements focusing on oxide−metal VANs.[58] These VAN systems offer a versatile combination of materials as well as the ability to tailor the density and dimensions of the metal pillars. Furthermore, oxide−metal VANs are particularly attractive due to their ease of fabrication, a wide range of applicable material combinations, and the capability to tune the film morphology to meet specific requirements. As an earlier example, BaTiO$_3$−Au (BTO−Au) shows strong optical anisotropy, high thermal stability, great tunability of pillar dimension and density, and potential integration with Si and flexible substrates.[59−63] In contrast to methodologies involving the exploitation of phase boundaries in oxide−oxide vertical arrangement nanoscale (VAN) systems, which necessitate elevated growth temperatures surpassing 800 °C coupled with stringent epitaxial growth requirements, the BTO−Au system presents an alternative approach.[64,65] This system can be cultivated at notably lower growth temperatures, below 600 °C, with potential for further reduction while also enabling seamless integration with diverse amorphous switching materials such as HfO$_2$. This simplified fabrication process of the BTO−Au system greatly enhances its potential for diverse applications.

In this work, we demonstrate a facile and effective electric-field-driven conducting filament formation using self-assembled uniform Au nanoelectrodes in an HfO$_2$ resistive switching device as artificial neurons. As illustrated in Figure 1a,b, the proposed device structure and the measurement setup, such uniform Au nanoelectrodes are embedded in the BTO matrix and underneath the HfO$_2$ switching layer to achieve controlled Ag filament growth and reduced threshold voltage. Figure 1 shows the cross-sectional schematic of the device. A self-assembled BTO−Au layer is deposited on top of the SrRuO$_3$ (SRO) bottom electrode, followed by the growth of the HfO$_2$ switching layer. The fabrication procedures are demonstrated in Figure S1. As evidenced in the COMSOL electric field simulation (Figure 1e,f), the one with Au

nanoelectrodes will provide a higher (∼1.8×) electric field near the Au electrode regions and thus achieve the selective Ag filament formation, which could significantly reduce the threshold voltage. Additionally, by comparing Figures 1c and 1d, we propose that the implementation of a BTO insulating matrix can lead to a greater stability and reduced formation of conducting filaments at undesired locations in comparison to pure HfO$_2$ devices. This results in lower energy consumption for the BTO-based devices. Details about the COMSOL simulation can be found in Supporting Information Section S2. This study presents a new approach to integrate vertically aligned nanocomposites with resistive switching materials, providing a new defect engineering approach to effectively improve device reliability and reduce energy consumption.

The detailed structural characterization of the HfO$_2$/BTO−Au stack was conducted using transmission electron microscopy (TEM) and scanning transmission electron microscopy (STEM) coupled with energy-dispersive spectroscopy (EDS) elementary mapping on a HfO$_2$/BTO−Au/STO reference sample, as shown in Figure 2a−c, respectively.
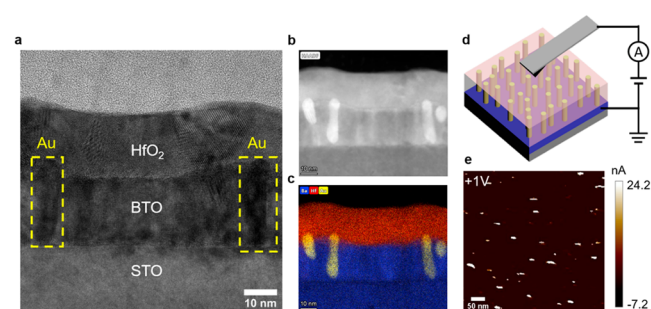


**Figure 2.** (a) TEM image of the HfO$_2$/BTO−Au film on STO substrate; Au nanoelectrodes are marked by yellow boxes in the image. (b, c) STEM and EDS mapping of the same region, showing the morphology and distribution of the Au nanoelectrodes. (d) Schematic illustration of the c-AFM measurement setup of the BTO−Au/SRO/STO sample. (e) c-AFM measurement results with 1 V applied to the sample. Bright spots indicate the Au nanoelectrodes.
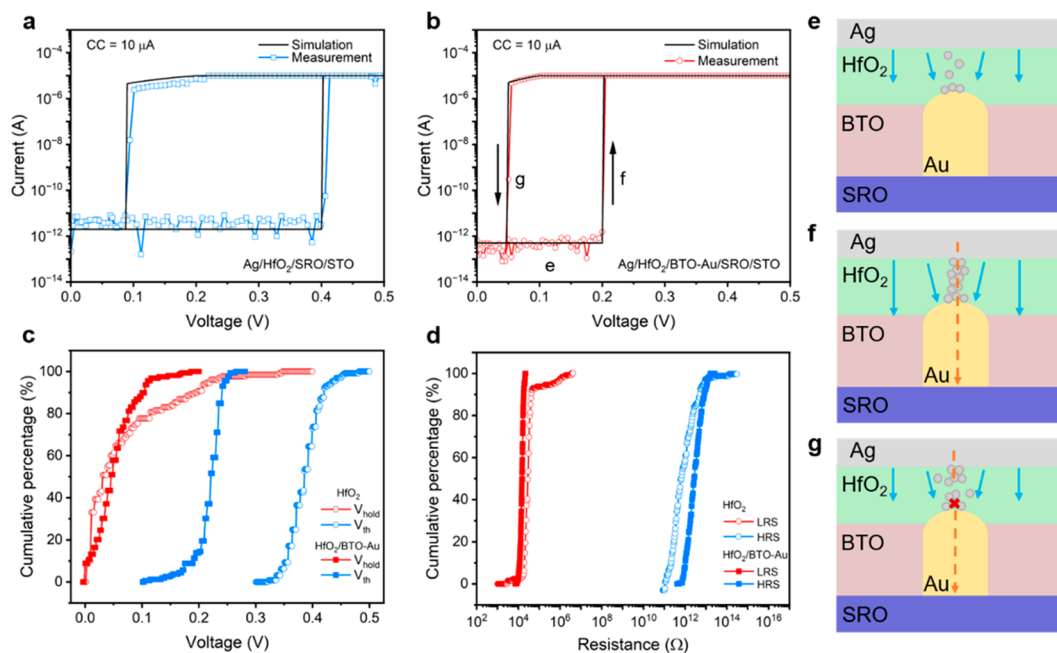
**Figure 3.** $I-V$ characteristics under DC stress and the simulation result of (a) the Ag/HfO$_2$/SRO/STO device and (b) the Ag/HfO$_2$/BTO−Au/SRO/STO device with 10 $\mu$A compliance current (CC). (c) Cumulative percentages of the hold (red curves) and threshold (blue curves) voltages of the HfO$_2$ and HfO$_2$/BTO−Au devices. (d) Cumulative percentages of the LRS (red curves) and HRS (blue curves) of the HfO$_2$ and HfO$_2$/BTO−Au devices. (e−g) Detailed schematic illustrations of the switching processes of different stages marked on the $I-V$ curve in (b).

Vertical Au nanopillars inside the crystalline BTO matrix connecting the polycrystalline HfO$_2$ layer with the STO substrate can be clearly identified. This pillar-in-matrix growth of the BTO−Au system originates from the difference in surface energies between Au and the oxides. Consequently, Au adatoms nucleate into islands (i.e., 3D growth mode) to minimize the surface energy of the metal phase, while the BTO adatoms grow in layer-by-layer (i.e., 2D growth mode) fashion, forming the overall pillar-in-matrix structure.[59] The Au nanoelectrodes, which extend a few nanometers into the HfO$_2$ layer, align with the structural design depicted in Figure 1. In addition to the desirable Au nanoelectrodes that penetrate the BTO matrix, smaller Au nanoparticles without complete pillar formation are also observed in Figure 2b,c. However, these nanoparticles do not contribute to the direct conduction path to the bottom electrode during the switching process. Such issue can potentially be circumvented by optimizing the growth conditions including the substrate temperature and laser energy as well as reducing the film thickness to reduce the chance of random Au nucleation during growth.[61,62] In order to reveal the distribution of the Au nanoelectrodes, conductive AFM (c-AFM) was performed on a BTO−Au/SRO/STO sample. Figure 2 illustrates the experimental setup of the c-AFM measurement. When the tip probes come into contact with the sample surface, only the regions containing the desired Au nanoelectrodes exhibit direct conduction, while areas with Au nanoparticles or without Au embedment remain insulating. The c-AFM result is shown in Figure 2e under a 1 V applied voltage. Bright spots with current up to 24 nA are shown, indicating the locations of ideal Au nanoelectrodes. Figure S2 presents XRD characterizations of three samples prepared for electrical measurements: HfO$_2$/SRO/STO (termed HfO$_2$), HfO$_2$/BTO−Au/SRO/STO (termed HfO$_2$/BTO−Au), and HfO$_2$/BTO/SRO/STO (termed HfO$_2$/BTO). Au nanostructures can be found for

the HfO$_2$/BTO−Au sample, confirming the existence of Au nanoelectrodes. Besides, no HfO$_2$ peak is shown in the XRD plots for all three samples, indicating polycrystalline/amorphous HfO$_2$. Detailed TEM and STEM images of the HfO$_2$/BTO−Au and HfO$_2$/BTO samples are shown in Figure S3. The measured thickness of the HfO$_2$ layer in both samples is approximately 10 nm. Uniformity in HfO$_2$ thickness across all three samples was achieved by employing an identical growth recipe (calibrated from the HfO$_2$/BTO−Au growth shown in Figure 2a) for HfO$_2$ deposition. Slightly increased Au nanoelectrode sizes in the sample grown on SRO is potentially due to the reduced vertical strain between BTO and Au.[66]

After depositions, square Ag top electrodes with dimensions of 10 $\mu$m and a 60 nm thickness were fabricated via e-beam evaporation and e-beam lithography. The electrical characteristics of the fabricated devices were evaluated using the experimental setup depicted in Figure 1a. In this configuration, the metallic SRO bottom electrode was grounded and a sweeping voltage was applied to the Ag top electrode. The SRO electrode has a work function similar to that of Au (approximately 5.2 eV), ensuring satisfactory ohmic contact with the Au nanoelectrodes.[67] The Ag electrode, on the other hand, has a work function of approximately 4.7 eV, which is approximately 0.5 eV lower than that of SRO. The ohmic contact and a contact resistance of approximately 125 $\Omega$ were revealed by the current−voltage ($I-V$) measurement of the Ag/SRO contact (see Figure S4). The $I-V$ characteristics of HfO$_2$ threshold switching devices with and without the BTO−Au buffer layer are presented in Figures 3a and 3b, alongside simulation results, respectively. Both devices exhibit threshold switching within the voltage sweep range of 0−0.5 V, characterized by sudden changes in current levels. These transitions correspond to the formation and rupture of Ag filaments, respectively, under a compliance current (CC) of 10 $\mu$A. The high-resistance state (HRS) of both devices lies

C

beyond the detection limit of the instrument, which is approximately picoamperes (~pA). This indicates excellent insulating properties of the 10 nm $HfO_2$ switching layer. 200 consecutive $I-V$ cycles on each sample were measured to gain insights into the stability and the statistical distribution of the hold voltage ($V_{hold}$) and threshold voltage ($V_{th}$), the resistances of the HRS, and the low-resistance state (LRS), as shown in Figure 3c,d. According to the results shown in Figure 3c, the mean values and standard deviations of $V_{hold}$ and $V_{th}$ are summarized in Table 1. The ratio of electric field strengths in

**Table 1. Statistics of $V_{th}$ and $V_{hold}$ for the $HfO_2$ and $HfO_2$/ BTO−Au Devices**

| device structure | threshold voltage (V) | hold voltage (V) |
|---|---|---|
| $HfO_2$ | 0.39 ± 0.03 | 0.07 ± 0.08 |
| $HfO_2$/BTO−Au | 0.22 ± 0.03 | 0.05 ± 0.04 |

$HfO_2$ with and without the Au nanoelectrodes (~1.8, indicated in Figure 1e,f) corresponds to the inverse of the two threshold voltages (~1.77). This observation suggests that the concentrated electric field at the Au nanoelectrodes is the main factor responsible for the lower threshold voltage (~0.22 V) observed in the $HfO_2$/BTO−Au device, as compared to the $HfO_2$ device ($V_{th}$ ~ 0.39 V). Furthermore, the $HfO_2$/BTO−Au device exhibits a tighter distribution and a smaller $V_{hold}$ (~0.05 V) in comparison to the $HfO_2$ device ($V_{hold}$ ~ 0.07 V),

indicating better stability and reliability of the device. The observed narrower $V_{hold}$ distribution in the $HfO_2$/BTO−Au device may be attributed to a more consistent distribution of Ag filament dimensions, particularly in terms of width. This phenomenon aligns with the proposed explanation by Wang et al., which suggests that the rupture of Ag filaments is a spontaneous relaxation process driven by surface energy minimization.[18,26] In contrast, the variability in Ag filament dimensions is likely more pronounced in the $HfO_2$ device where there is limited control over the filament formation process. The low $V_{th}$ achieved in the 10 nm thick $HfO_2$/BTO− Au device is comparable with the results reported in the 5 nm thick ALD growth $HfO_2$ device.[24,68] A thicker $HfO_2$ film with low $V_{th}$ is beneficial for device applications as it provides an even lower leakage current, reducing the energy consumption.

Moreover, the $IV$ characteristics of the $HfO_2$/BTO control sample with no Au nanoelectrodes show capacitive behavior for 0−2 V sweep (Figure S5a) and a transition in resistance at approximately 2.3 V (Figure S5b). The observed characteristics in the control sample provide evidence against the involvement of BTO's ferroelectricity in threshold switching and reinforce the filtering effect (as discussed in Supporting Information Section 2) of the BTO buffer layer when scanning at lower voltages (0−0.5 V). Additionally, a previous study of ferroelectric BTO memristors with smaller thicknesses (<10 nm) has shown higher switching voltages (~2 V), which
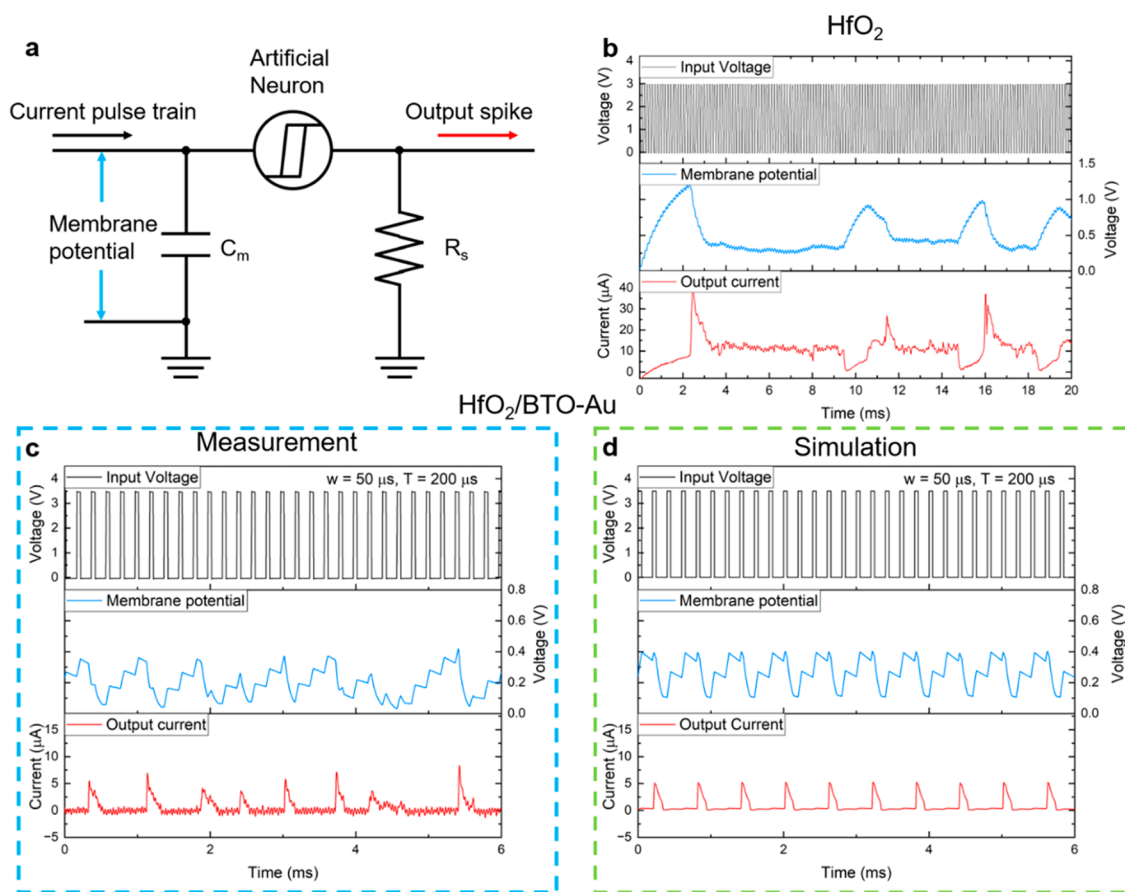


**Figure 4.** (a) Schematic illustration of the leaky integrate-and-fire circuit. (b) The firing behavior of the Ag/$HfO_2$ device when subject to an input voltage pulse train with 3 V, 50 $\mu$s width, and 100 $\mu$s period. (c) Measurement results and (d) simulation results of the Ag/$HfO_2$/BTO−Au device under an input voltage pulse train with 3.5 V, 50 $\mu$s width, and 200 $\mu$s period.

supports the conclusion that ferroelectricity does not play a role in threshold switching.[69]

Figure 3e−g provides schematic representations of the formation and rupture of Ag filaments during the resistive switching process in the $HfO_2$/BTO−Au device, specifically in the three distinct sections marked in Figure 3b. Initially, the Ag atoms located in the upper electrode underwent ionization. Consequently, the resulting $Ag^+$ ions migrated toward the Au nanoelectrodes. Subsequently, these $Ag^+$ ions underwent a reduction process facilitated by electron capture, leading to the formation of the foundational structure for Ag filaments.[70,71] The presence of Au nanoelectrodes in the $HfO_2$/BTO−Au device results in a lower $V_{th}$, leading to the formation of Ag filaments with significantly smaller dimensions compared to those formed at higher voltages in the $HfO_2$ device. Consequently, Ag filament rupture likely caused by unstable Ag ions occurs more easily in filaments with smaller dimensions.[72] In contrast, the higher $V_{th}$ of the $HfO_2$ device leads to the formation of thicker and denser Ag filaments that are harder to dissolve, resulting in unwanted nonvolatility of the device and an inability to switch back to the HRS even under low or no applied electric field.

Artificial neurons are of utmost importance in the field of neuromorphic computing, as they facilitate data processing. Within spiking neural networks (SNN), these neurons are responsible for receiving input data in the form of pulses and subsequently generating output pulses once the voltage surpasses a predefined threshold.[73] This behavior closely resembles the action potential generation observed in biological neurons. To accurately replicate the action potential generation exhibited by biological neurons, the leaky integrate-and-fire (LIF) neuron model is widely adopted within the field of neuromorphic computing. LIF measurements were conducted to verify the functionality of the threshold switching devices as artificial neurons, as illustrated in Figure 4a. The membrane potential was determined to be the voltage drop across the membrane capacitance, which was represented by capacitor $C_m$. The threshold switching devices functioned as artificial neurons, switching between the HRS and the LRS once the membrane potential reached the desired levels.[74] A shunt resistor $R_s$ was connected in series with the artificial neuron to facilitate measurement of the output current. In the actual circuit, a capacitor of 1 nF and a shunt resistor of 10 kΩ were utilized (see the Supporting Information, Section S7). The input voltage pulses from the wave generator were converted to current pulses by using a customized Howland current pump before being input into the measurement circuit.

Figure 4b illustrates the firing behavior of the $HfO_2$ device without Au nanoelectrodes. With input voltage pulses of 3 V, which were converted to approximately 3 μA current pulses by the Howland current pump with a width of 50 μs and a period of 100 μs, the firing of the $HfO_2$ device was shown to be inconsistent throughout the 20 ms measurement period. The voltage required to trigger the firing varied from 0.9 to 1.2 V. A longer period of 200 μs and 3.5 V input voltage did not trigger the firing of the $HfO_2$ device, as the membrane potential failed to exceed 0.9 V (see Figure S7). In addition, large leakage current (∼10 μA) was observed between consecutive firing events, with the membrane potential remaining at approximately 0.4 V. This suggests that the device remained in the LRS of 30 kΩ and failed to switch back to the HRS immediately after firing.

In contrast, the $HfO_2$/BTO−Au devices demonstrated more consistent performance under low triggering potentials (<0.4 V), as depicted in Figure 4c. Moreover, these devices exhibited negligible leakage current between firing events, indicating an immediate transition from the LRS back to the HRS and considerably lower energy consumption for neuromorphic computing applications. The statistical results of the $V_{th}$ distribution derived from LIF measurements from 10 different $HfO_2$/BTO−Au devices are presented in Figure S8. The overall $V_{th}$ extracted from all of the measurements was found to be 0.31 ± 0.07 V, which is slightly higher than the $V_{th}$ derived from the $I-V$ characteristics. The simulation results of the artificial neuron (with $V_{th}$ = 0.4 V, $V_{hold}$ = 0.05 V, LRS = 70 kΩ, HRS = 10 GΩ) are shown in Figure 4d, with the magnitude and pulse interval in good agreement with the experimental results, thus confirming the stability of the $HfO_2$/BTO−Au artificial neurons.

In summary, $HfO_2$ artificial neurons with embedded Au nanoelectrodeshave been fabricated by inserting a self-assembled VAN BTO−Au buffer layer for the first time. The novelty of the Au nanoelectrodes in the VAN buffer layer lies in the following: (1) the Au nanoelectrodes provide spatial control and enhanced electric field in the $HfO_2$ switching layer that not only reduce the threshold switching voltage but also improve the stability of the device in both threshold switching characteristics and neuron functionality; (2) the insulating BTO matrix serves as a filter layer, eliminating the unwanted filament formation and minimizing the impact of defects in the $HfO_2$ switching layer; and (3) the fabrication of artificial neurons can be achieved in a consecutive thin film growth session without any postdeposition processing, which significantly reduces the number of steps involved and improves the feasibility of future device implementation. While the devices in this study were deposited on STO substrates, they can be integrated onto Si substrates by initially depositing a set ofbuffer layers, e.g., TiN/STO. Further tunability in the dimension and distribution of Au nanoelectrodes as well as other metal electrode selections opens up versatile design potential for future switching devices with specific device density, functionality, and energy-efficiency requirements. Within this innovative framework, the extensive repertoire of VANs emerges as a valuable resource, offering a multitude of potential VAN selections. These systems hold the promise of imbuing integrated devices with a wide range of functionalities encompassing optical and magnetic properties. This transformative potential not only facilitates seamless multifunctional integration but also opens exciting prospects for exploring synergistic couplings between distinct physical properties toward future device schemes.

## ■ ASSOCIATED CONTENT

**ⓈⒾ Supporting Information**

The Supporting Information is available free of charge at https://pubs.acs.org/doi/10.1021/acs.nanolett.3c02217.

> Additional details on XRD, TEM, measurement setup, and electrical measurements (PDF)

## ■ AUTHOR INFORMATION

**Corresponding Authors**

   **Hongyi Dou** − *School of Materials Engineering, Purdue University, West Lafayette, Indiana 47907, United States*; Email: douh@purdue.edu

**Haiyan Wang** − *School of Materials Engineering and Elmore School of Electrical Engineering, Purdue University, West Lafayette, Indiana 47907, United States;* ⬤ orcid.org/0000-0002-7397-1209; Email: hwang00@purdue.edu

## Authors

**Zehao Lin** − *Elmore School of Electrical Engineering, Purdue University, West Lafayette, Indiana 47907, United States*

**Zedong Hu** − *Elmore School of Electrical Engineering, Purdue University, West Lafayette, Indiana 47907, United States*

**Benson Kunhung Tsai** − *School of Materials Engineering, Purdue University, West Lafayette, Indiana 47907, United States*

**Dongqi Zheng** − *Elmore School of Electrical Engineering, Purdue University, West Lafayette, Indiana 47907, United States*

**Jiawei Song** − *School of Materials Engineering, Purdue University, West Lafayette, Indiana 47907, United States*

**Juanjuan Lu** − *School of Materials Engineering, Purdue University, West Lafayette, Indiana 47907, United States*

**Xinghang Zhang** − *School of Materials Engineering, Purdue University, West Lafayette, Indiana 47907, United States;* ⬤ orcid.org/0000-0002-8380-8667

**Quanxi Jia** − *Department of Materials Design and Innovation, School of Engineering and Applied Sciences, University at Buffalo, The State University of New York, Buffalo, New York 14260, United States*

**Judith L. MacManus-Driscoll** − *Department of Material Science & Metallurgy, University of Cambridge, Cambridge CB3 0FS, United Kingdom;* ⬤ orcid.org/0000-0003-4987-6620

**Peide D. Ye** − *Elmore School of Electrical Engineering, Purdue University, West Lafayette, Indiana 47907, United States;* ⬤ orcid.org/0000-0001-8466-9745

Complete contact information is available at:
https://pubs.acs.org/10.1021/acs.nanolett.3c02217

## Author Contributions

H.D. and H.W. conceived the project. H.D. designed the experimental work. H.D. conducted PLD depositions with the help of J.L. and performed structural analysis including TEM and XRD. Z.L. and D.Z. fabricated the devices. Z.L. and H.D. did electrical measurements on the fabricated devices. Z.H. prepared the TEM samples. B.T. performed c-AFM on the samples. J.S. helped with graphic designs of the paper. H.D. and Z.L. analyzed the data and discussed the results. H.D. and H.W. wrote the manuscript with the comments and improvements from all coauthors. X.Z., J.L. M.-D., and Q.X.J. commented on the research as it progressed. H.W. acquired funding and supervised the research.

## Notes

The authors declare no competing financial interest.

## ■ REFERENCES

(1) Schuman, C. D.; Kulkarni, S. R.; Parsa, M.; Mitchell, J. P.; Date, P.; Kay, B. Opportunities for Neuromorphic Computing Algorithms and Applications. *Nat. Comput. Sci.* **2022**, 2 (1), 10−19.

(2) Zhang, W.; Gao, B.; Tang, J.; Yao, P.; Yu, S.; Chang, M. F.; Yoo, H. J.; Qian, H.; Wu, H. Neuro-Inspired Computing Chips. *Nat. Electron.* **2020**, 3 (7), 371−382.

(3) Tang, J.; Yuan, F.; Shen, X.; Wang, Z.; Rao, M.; He, Y.; Sun, Y.; Li, X.; Zhang, W.; Li, Y.; Gao, B.; Qian, H.; Bi, G.; Song, S.; Yang, J. J.; Wu, H. Bridging Biological and Artificial Neural Networks with Emerging Neuromorphic Devices: Fundamentals, Progress, and Challenges. *Adv. Mater.* **2019**, 31 (49), 1902761.

(4) Burr, G. W.; Shelby, R. M.; Sebastian, A.; Kim, S.; Kim, S.; Sidler, S.; Virwani, K.; Ishii, M.; Narayanan, P.; Fumarola, A.; Sanches, L. L.; Boybat, I.; Le Gallo, M.; Moon, K.; Woo, J.; Hwang, H.; Leblebici, Y. Neuromorphic Computing Using Non-Volatile Memory. *Adv. Phys. X* **2017**, 2 (1), 89−124.

(5) Upadhyay, N. K.; Jiang, H.; Wang, Z.; Asapu, S.; Xia, Q.; Joshua Yang, J. Emerging Memory Devices for Neuromorphic Computing. *Adv. Mater. Technol.* **2019**, 4 (4), 1−13.

(6) Si, M.; Luo, Y.; Chung, W.; Bae, H.; Zheng, D.; Li, J.; Qin, J.; Qiu, G.; Yu, S.; Ye, P. D. A Novel Scalable Energy-Efficient Synaptic Device: Crossbar Ferroelectric Semiconductor Junction. *2019 IEEE International Electron Devices Meeting (IEDM)* **2019**, 2, 6.6.1−6.6.4.

(7) Yang, J. J.; Pickett, M. D.; Li, X.; Ohlberg, D. A. A.; Stewart, D. R.; Williams, R. S. Memristive Switching Mechanism for Metal/Oxide/Metal Nanodevices. *Nat. Nanotechnol.* **2008**, 3 (7), 429−433.

(8) Gale, E. TiO₂-Based Memristors and ReRAM: Materials, Mechanisms and Models (a Review). *Semicond. Sci. Technol.* **2014**, 29 (10), 104004.

(9) Yang, J. J.; Zhang, M. X.; Strachan, J. P.; Miao, F.; Pickett, M. D.; Kelley, R. D.; Medeiros-Ribeiro, G.; Williams, R. S. High Switching Endurance in TaOx Memristive Devices. *Appl. Phys. Lett.* **2010**, 97 (23), 6−9.

(10) Zhang, J.; Zhao, H.; Wei, F.; Yang, M.; Yang, Z.; Chen, Q.; Chen, J. Resistive Switching Behaviour of Highly Epitaxial CeO₂ Thin Film for Memory Application. *Phys. Status Solidi - Rapid Res. Lett.* **2014**, 8 (1), 95−99.

(11) Huang, P.; Wang, Y.; Li, H.; Gao, B.; Chen, B.; Zhang, F.; Zeng, L.; Du, G.; Kang, J.; Liu, X. Analysis of the Voltage-Time Dilemma of Metal Oxide-Based Rram and Solution Exploration of High Speed and Low Voltage Ac Switching. *IEEE Trans. Nanotechnol.* **2014**, 13 (6), 1127−1132.

(12) Xie, S.; Pei, L.; Li, M.; Zhu, Y.; Cheng, X.; Ding, H.; Xiong, R. Light-Controlled Resistive Switching and Voltage-Controlled Photoresponse Characteristics in the Pt/CeO₂/Nb:SrTiO3 Heterostructure. *J. Alloys Compd.* **2019**, 778, 141−147.

(13) Brivio, S.; Spiga, S.; Ielmini, D. HfO₂-Based Resistive Switching Memory Devices for Neuromorphic Computing. *Neuromorphic Comput. Eng.* **2022**, 2 (4), No. 042001.

(14) Bousoulas, P.; Sakellaropoulos, D.; Tsoukalas, D. Tuning the Analog Synaptic Properties of Forming Free SiO₂memristors by Material Engineering. *Appl. Phys. Lett.* **2021**, 118 (14), 143502.

(15) Ilyas, N.; Li, C.; Wang, J.; Jiang, X.; Fu, H.; Liu, F.; Gu, D.; Jiang, Y.; Li, W. A Modified SiO₂-Based Memristor with Reliable Switching and Multifunctional Synaptic Behaviors. *J. Phys. Chem. Lett.* **2022**, 13 (3), 884−893.

(16) Fowler, B. W.; Chang, Y. F.; Zhou, F.; Wang, Y.; Chen, P. Y.; Xue, F.; Chen, Y. T.; Bringhurst, B.; Pozder, S.; Lee, J. C. Electroforming and Resistive Switching in Silicon Dioxide Resistive Memory Devices. *RSC Adv.* **2015**, 5 (27), 21215−21236.

(17) Jo, S. H.; Chang, T.; Ebong, I.; Bhadviya, B. B.; Mazumder, P.; Lu, W. Nanoscale Memristor Device as Synapse in Neuromorphic Systems. *Nano Lett.* **2010**, 10 (4), 1297−1301.

(18) Wang, Z.; Joshi, S.; Savel'ev, S. E.; Jiang, H.; Midya, R.; Lin, P.; Hu, M.; Ge, N.; Strachan, J. P.; Li, Z.; Wu, Q.; Barnell, M.; Li, G. L.;

Xin, H. L.; Williams, R. S.; Xia, Q.; Yang, J. J. Memristors with Diffusive Dynamics as Synaptic Emulators for Neuromorphic Computing. *Nat. Mater.* **2017**, *16* (1), 101−108.

(19) Waser, R.; Aono, M. Nanoionics-Based Resistive Switching Memories. *Nanosci. Technol. A Collect. Rev. from Nat. Journals* **2009**, 158−165.

(20) Ielmini, D. Resistive Switching Memories Based on Metal Oxides: Mechanisms, Reliability and Scaling. *Semicond. Sci. Technol.* **2016**, *31* (6), 063002.

(21) Ielmini, D. Brain-Inspired Computing with Resistive Switching Memory (RRAM): Devices, Synapses and Neural Networks. *Microelectron. Eng.* **2018**, *190*, 44−53.

(22) Wang, Z.; Wu, H.; Burr, G. W.; Hwang, C. S.; Wang, K. L.; Xia, Q.; Yang, J. J. Resistive Switching Materials for Information Processing. *Nat. Rev. Mater.* **2020**, *5* (3), 173−195.

(23) Wang, Z.; Rao, M.; Midya, R.; Joshi, S.; Jiang, H.; Lin, P.; Song, W.; Asapu, S.; Zhuo, Y.; Li, C.; Wu, H.; Xia, Q.; Yang, J. J. Threshold Switching of Ag or Cu in Dielectrics: Materials, Mechanism, and Applications. *Adv. Funct. Mater.* **2018**, *28* (6), 1704862.

(24) Hua, Q.; Wu, H.; Gao, B.; Zhao, M.; Li, Y.; Li, X.; Hou, X.; Chang, M. F.; Zhou, P.; Qian, H. A Threshold Switching Selector Based on Highly Ordered Ag Nanodots for X-Point Memory Applications. *Adv. Sci.* **2019**, *6* (10), 1902761.

(25) Song, M.; Lee, S.; Nibhanupudi, S. S. T.; Singh, J. V.; Disiena, M.; Luth, C. J.; Wu, S.; Coupin, M. J.; Warner, J. H.; Banerjee, S. K. Self-Compliant Threshold Switching Devices with High On/Off Ratio by Control of Quantized Conductance in Ag Filaments. *Nano Lett.* **2023**, *23*, 2−7.

(26) Midya, R.; Wang, Z.; Zhang, J.; Savel'ev, S. E.; Li, C.; Rao, M.; Jang, M. H.; Joshi, S.; Jiang, H.; Lin, P.; Norris, K.; Ge, N.; Wu, Q.; Barnell, M.; Li, Z.; Xin, H. L.; Williams, R. S.; Xia, Q.; Yang, J. J. Anatomy of Ag/Hafnia-Based Selectors with 1010 Nonlinearity. *Adv. Mater.* **2017**, *29* (12), 1−8.

(27) Zidan, M. A.; Strachan, J. P.; Lu, W. D. The Future of Electronics Based on Memristive Systems. *Nat. Electron.* **2018**, *1* (1), 22−29.

(28) Sung, C.; Hwang, H.; Yoo, I. K. Perspective: A Review on Memristive Hardware for Neuromorphic Computation. *J. Appl. Phys.* **2018**, *124* (15), 151903.

(29) Li, T.; Yu, H.; Chen, S. H. Y.; Zhou, Y.; Han, S. T. The Strategies of Filament Control for Improving the Resistive Switching Performance. *J. Mater. Chem. C* **2020**, *8* (46), 16295−16317.

(30) Islam, R.; Li, H.; Chen, P. Y.; Wan, W.; Chen, H. Y.; Gao, B.; Wu, H.; Yu, S.; Saraswat, K.; Philip Wong, H. S. Device and Materials Requirements for Neuromorphic Computing. *J. Phys. D. Appl. Phys.* **2019**, *52* (11), 113001.

(31) Lanza, M.; Zhang, K.; Porti, M.; Nafria, M.; Shen, Z. Y.; Liu, L. F.; Kang, J. F.; Gilmer, D.; Bersuker, G. Grain Boundaries as Preferential Sites for Resistive Switching in the HfO 2 Resistive Random Access Memory Structures. *Appl. Phys. Lett.* **2012**, *100* (12), 123508.

(32) Petzold, S.; Zintler, A.; Eilhardt, R.; Piros, E.; Kaiser, N.; Sharath, S. U.; Vogel, T.; Major, M.; McKenna, K. P.; Molina-Luna, L.; Alff, L. Forming-Free Grain Boundary Engineered Hafnium Oxide Resistive Random Access Memory Devices. *Adv. Electron. Mater.* **2019**, *5* (10), No. 1900484.

(33) Szot, K.; Speier, W.; Bihlmayer, G.; Waser, R. Switching the Electrical Resistance of Individual Dislocations in Single-Crystalline SrTiO3. *Nat. Mater.* **2006**, *5* (4), 312−320.

(34) Adepalli, K. K.; Yang, J.; Maier, J.; Tuller, H. L.; Yildiz, B. Tunable Oxygen Diffusion and Electronic Conduction in SrTiO3 by Dislocation-Induced Space Charge Fields. *Adv. Funct. Mater.* **2017**, *27* (22), 1−9.

(35) Dou, H.; Hellenbrand, M.; Xiao, M.; Hu, Z.; Kunwar, S.; Chen, A.; MacManus-Driscoll, J. L.; Jia, Q.; Wang, H. Engineering of Grain Boundaries in CeO 2 Enabling Tailorable Resistive Switching Properties. *Adv. Electron. Mater.* **2023**, *9* (5), No. 201186.

(36) Ge, J.; Chaker, M. Oxygen Vacancies Control Transition of Resistive Switching Mode in Single-Crystal TiO2Memory Device. *ACS Appl. Mater. Interfaces* **2017**, *9* (19), 16327−16334.

(37) Rana, A. M.; Akbar, T.; Ismail, M.; Ahmad, E.; Hussain, F.; Talib, I.; Imran, M.; Mehmood, K.; Iqbal, K.; Nadeem, M. Y. Endurance and Cycle-to-Cycle Uniformity Improvement in Tri-Layered CeO 2 /Ti/CeO 2 Resistive Switching Devices by Changing Top Electrode Material. *Sci. Rep.* **2017**, *7*, 1−15.

(38) Zhao, Q.; Zhou, M.; Zhang, W.; Liu, Q.; Li, X.; Liu, M.; Dai, Y. Effects of Interaction between Defects on the Uniformity of Doping HfO 2-Based RRAM: A First Principle Study. *J. Semicond.* **2013**, *34* (3), 032001.

(39) Sedghi, N.; Li, H.; Brunell, I. F.; Dawson, K.; Guo, Y.; Potter, R. J.; Gibbon, J. T.; Dhanak, V. R.; Zhang, W. D.; Zhang, J. F.; Hall, S.; Robertson, J.; Chalker, P. R. Enhanced Switching Stability in Ta 2 O 5 Resistive RAM by Fluorine Doping. *Appl. Phys. Lett.* **2017**, *111* (9), No. 092904.

(40) Traore, B.; Blaise, P.; Vianello, E.; Grampeix, H.; Jeannot, S.; Perniola, L.; De Salvo, B.; Nishi, Y. On the Origin of Low-Resistance State Retention Failure in HfO2-Based RRAM and Impact of Doping/Alloying. *IEEE Trans. Electron Devices* **2015**, *62* (12), 4029−4036.

(41) Wang, Z.; Zhu, W. G.; Du, A. Y.; Wu, L.; Fang, Z.; Tran, X. A.; Liu, W. J.; Zhang, K. L.; Yu, H. Y. Highly Uniform, Self-Compliance, and Forming-Free ALD HfO 2-Based RRAM with Ge Doping. *IEEE Trans. Electron Devices* **2012**, *59* (4), 1203−1208.

(42) Tan, T.; Guo, T.; Chen, X.; Li, X.; Liu, Z. Impacts of Au-Doping on the Performance of Cu/HfO 2 /Pt RRAM Devices. *Appl. Surf. Sci.* **2014**, *317*, 982−985.

(43) Tappertzhofen, S.; Hofmann, S. Embedded Nanoparticle Dynamics and Their Influence on Switching Behaviour of Resistive Memory Devices. *Nanoscale* **2017**, *9* (44), 17494−17504.

(44) Han, U.-B.; Lee, J.-S. Bottom-up Synthesis of Ordered Metal/Oxide/Metal Nanodots on Substrates for Nanoscale Resistive Switching Memory. *Sci. Rep.* **2016**, *6*, 1−8.

(45) Au, K.; Gao, X. S.; Wang, J.; Bao, Z. Y.; Liu, J. M.; Dai, J. Y. Enhanced Resistive Switching Effect in Ag Nanoparticle Embedded BaTiO 3 Thin Films. *J. Appl. Phys.* **2013**, *114* (2), 027019.

(46) Song, J. M.; Lee, J. S. Self-Assembled Nanostructured Resistive Switching Memory Devices Fabricated by Templated Bottom-up Growth. *Sci. Rep.* **2016**, *6*, 1−7.

(47) Wang, J.; Li, L.; Huyan, H.; Pan, X.; Nonnenmann, S. S. Highly Uniform Resistive Switching in HfO2 Films Embedded with Ordered Metal Nanoisland Arrays. *Adv. Funct. Mater.* **2019**, DOI: 10.1002/adfm.201808430.

(48) Liu, Q.; Long, S.; Lv, H.; Wang, W.; Niu, J.; Huo, Z.; Chen, J.; Liu, M. Controllable Growth of Nanoscale Conductive Filaments in Solid-Electrolyte-Based ReRAM by Using a Metal Nanocrystal Covered Bottom Electrode. *ACS Nano* **2010**, *4* (10), 6162−6168.

(49) Huang, Y. C.; Tsai, W. L.; Chou, C. H.; Wan, C. Y.; Hsiao, C.; Cheng, H. C. High-Performance Programmable Metallization Cell Memory with the Pyramid-Structured Electrode. *IEEE Electron Device Lett.* **2013**, *34* (10), 1244−1246.

(50) Shin, K. Y.; Kim, Y.; Antolinez, F. V.; Ha, J. S.; Lee, S. S.; Park, J. H. Controllable Formation of Nanofilaments in Resistive Memories via Tip-Enhanced Electric Fields. *Adv. Electron. Mater.* **2016**, *2* (10), 1−8.

(51) Spring, J.; Sediva, E.; Hood, Z. D.; Gonzalez-Rosillo, J. C.; O'Leary, W.; Kim, K. J.; Carrillo, A. J.; Rupp, J. L. M. Toward Controlling Filament Size and Location for Resistive Switches via Nanoparticle Exsolution at Oxide Interfaces. *Small* **2020**, *16* (41), 1−11.

(52) Wang, J.; Li, L.; Huyan, H.; Pan, X.; Nonnenmann, S. S. Highly Uniform Resistive Switching in HfO2 Films Embedded with Ordered Metal Nanoisland Arrays. *Adv. Funct. Mater.* **2019**, *29* (25), 1−11.

(53) Aimon, N. M.; Choi, H. K.; Sun, X. Y.; Kim, D. H.; Ross, C. A. Templated Self-Assembly of Functional Oxide Nanocomposites. *Adv. Mater.* **2014**, *26* (19), 3063−3067.

(54) Chen, A.; Su, Q.; Han, H.; Enriquez, E.; Jia, Q. Metal Oxide Nanocomposites: A Perspective from Strain, Defect, and Interface. *Adv. Mater.* **2019**, *31* (4), 1−30.

(55) Gao, X.; Zhang, D.; Wang, X.; Jian, J.; He, Z.; Dou, H.; Wang, H. Vertically Aligned Nanocomposite (BaTiO 3) 0.8 : (La 0.7 Sr 0.3 MnO 3) 0.2 Thin Films with Anisotropic Multifunctionalities. *Nanoscale Adv.* **2020**, *2* (8), 3276−3283.

(56) Dou, H.; Gao, X.; Zhang, D.; Dhole, S.; Qi, Z.; Yang, B.; Hasan, M. N.; Seo, J. H.; Jia, Q.; Hellenbrand, M.; MacManus-Driscoll, J. L.; Zhang, X.; Wang, H. Electroforming-Free $HfO_2:CeO_2$ Vertically Aligned Nanocomposite Memristors with Anisotropic Dielectric Response. *ACS Appl. Electron. Mater.* **2021**, *3* (12), 5278−5286.

(57) Enriquez, E.; Li, Q.; Bowlan, P.; Lu, P.; Zhang, B.; Li, L.; Wang, H.; Taylor, A. J.; Yarotski, D.; Prasankumar, R. P.; Kalinin, S. V.; Jia, Q.; Chen, A. Induced Ferroelectric Phases in SrTiO3by a Nanocomposite Approach. *Nanoscale* **2020**, *12* (35), 18193−18199.

(58) Misra, S.; Wang, H. Review on the Growth, Properties and Applications of Self-Assembled Oxide-Metal Vertically Aligned Nanocomposite Thin Films-Current and Future Perspectives. *Mater. Horizons* **2021**, *8* (3), 869−884.

(59) Li, L.; Sun, L.; Gomez-Diaz, J. S.; Hogan, N. L.; Lu, P.; Khatkhatay, F.; Zhang, W.; Jian, J.; Huang, J.; Su, Q.; Fan, M.; Jacob, C.; Li, J.; Zhang, X.; Jia, Q.; Sheldon, M.; Alù, A.; Li, X.; Wang, H. Self-Assembled Epitaxial Au-Oxide Vertically Aligned Nanocomposites for Nanoscale Metamaterials. *Nano Lett.* **2016**, *16* (6), 3936−3943.

(60) Misra, S.; Li, L.; Zhang, D.; Jian, J.; Qi, Z.; Fan, M.; Chen, H.; Zhang, X.; Wang, H. Self-Assembled Ordered Three-Phase Au−BaTiO 3 − ZnO Vertically Aligned Nanocomposites Achieved by a Templating Method. *Adv. Mater.* **2019**, *31* (7), No. 1806529.

(61) Zhang, D.; Misra, S.; Li, L.; Wang, X.; Jian, J.; Lu, P.; Gao, X.; Sun, X.; Qi, Z.; Kalaswad, M.; Zhang, X.; Wang, H. Tunable Optical Properties in Self-Assembled Oxide-Metal Hybrid Thin Films via Au-Phase Geometry Control: From Nanopillars to Nanodisks. *Adv. Opt. Mater.* **2020**, *8* (4), 1−10.

(62) Liu, J.; Wang, X.; Gao, X.; Wang, H.; Jian, J.; Huang, J.; Sun, X.; Qi, Z.; Misra, S.; He, Z.; Wang, H. Multifunctional Self-Assembled BaTiO3-Au Nanocomposite Thin Films on Flexible Mica Substrates with Tunable Optical Properties. *Appl. Mater. Today* **2020**, *21*, No. 100856.

(63) Kalaswad, M.; Zhang, D.; Gao, X.; Contreras, L. L.; Wang, H.; Wang, X.; Wang, H. Integration of Hybrid Plasmonic Au-BaTiO3Metamaterial on Silicon Substrates. *ACS Appl. Mater. Interfaces* **2019**, *11* (48), 45199−45206.

(64) Cho, S.; Yun, C.; Tappertzhofen, S.; Kursumovic, A.; Lee, S.; Lu, P.; Jia, Q.; Fan, M.; Jian, J.; Wang, H.; Hofmann, S.; MacManus-Driscoll, J. L. Self-Assembled Oxide Films with Tailored Nanoscale Ionic and Electronic Channels for Controlled Resistive Switching. *Nat. Commun.* **2016**, *7* (1), No. 12373.

(65) Lee, S.; Sangle, A.; Lu, P.; Chen, A.; Zhang, W.; Lee, J. S.; Wang, H.; Jia, Q.; MacManus-Driscoll, J. L. Novel Electroforming-Free Nanoscaffold Memristor with Very High Uniformity, Tunability, and Density. *Adv. Mater.* **2014**, *26* (36), 6284−6289.

(66) Chen, A.; Jia, Q. A Pathway to Desired Functionalities in Vertically Aligned Nanocomposites and Related Architectures. *MRS Bull.* **2021**, *46* (2), 115−122.

(67) Yoshida, C.; Yoshida, A.; Tamura, H. Nanoscale Conduction Modulation in Au/Pb(Zr, Ti)O3/SrRuO3 Heterostructure. *Appl. Phys. Lett.* **1999**, *75* (10), 1449−1451.

(68) Chekol, S. A.; Cuppers, F.; Waser, R.; Hoffmann-Eifert, S. An Ag/HfO2/Pt Threshold Switching Device with an Ultra-Low Leakage (< 10 FA), High On/OffRatio (> 1011), and Low Threshold Voltage (< 0.2 V) for Energy-Efficient Neuromorphic Computing. *2021 IEEE Int. Mem. Work. IMW 2021 - Proc.* **2021**, 2021−2024.

(69) Ma, C.; Luo, Z.; Huang, W.; Zhao, L.; Chen, Q.; Lin, Y.; Liu, X.; Chen, Z.; Liu, C.; Sun, H.; Jin, X.; Yin, Y.; Li, X. Sub-Nanosecond Memristor Based on Ferroelectric Tunnel Junction. *Nat. Commun.* **2020**, *11* (1), 1−9.

(70) Valov, I.; Waser, R.; Jameson, J. R.; Kozicki, M. N. Electrochemical Metallization Memories—Fundamentals, Applications, Prospects. *Nanotechnology* **2011**, *22* (25), 254003.

(71) Lu, W.; Jeong, D. S.; Kozicki, M.; Waser, R. Electrochemical Metallization Cells — Blending Nanoionics into Nanoelectronics ? *MRS Bull.* **2012**, *37*, 124−130.

(72) Chekol, S. A.; Menzel, S.; Ahmad, R. W.; Waser, R.; Hoffmann-Eifert, S. Effect of the Threshold Kinetics on the Filament Relaxation Behavior of Ag-Based Diffusive Memristors. *Adv. Funct. Mater.* **2022**, DOI: 10.1002/adfm.202111242.

(73) Li, Z. X.; Geng, X. Y.; Wang, J.; Zhuge, F. Emerging Artificial Neuron Devices for Probabilistic Computing. *Front. Neurosci.* **2021**, *15*, 1−18.

(74) Lee, D.; Kwak, M.; Moon, K.; Choi, W.; Park, J.; Yoo, J.; Song, J.; Lim, S.; Sung, C.; Banerjee, W.; Hwang, H. Various Threshold Switching Devices for Integrate and Fire Neuron Applications. *Adv. Electron. Mater.* **2019**, *5* (9), 1−7.